JVST A
Journal of Vacuum Science & Technology A

ARTICLE

avs.scitation.org/journal/jva

Spontaneous etching of B_2O_3 by HF gas studied using infrared spectroscopy, mass spectrometry, and density functional theory

Cite as: J. Vac. Sci. Technol. A 40, 022601 (2022); doi: 10.1116/6.0001542
Submitted: 8 October 2021 · Accepted: 10 December 2021 ·
Published Online: 11 January 2022

Austin M. Cano,[1] Suresh Kondati Natarajan,[2,3] Jonathan L. Partridge,[1] Simon D. Elliott,[4] and Steven M. George[1]

AFFILIATIONS

[1]Department of Chemistry, University of Colorado, Boulder, Colorado 80309
[2]University College Cork, Tyndall National Institute, Lee Maltings, Dyke Parade, Cork T12 R5CP, Ireland
[3]Department of Electrical Engineering and Automation, Aalto University, Espoo 02150, Finland
[4]Schrödinger Inc., 120 West 45th Street, 17th Floor, New York, New York 10036-4041

Note: This paper is part of the 2022 Special Topic Collection on Atomic Layer Etching (ALE)

ABSTRACT

The spontaneous etching of boron oxide (B_2O_3) by hydrogen fluoride (HF) gas is important during thermal atomic layer etching after BCl_3 converts the surface of various metal oxides to a B_2O_3 layer. In this study, the chemical vapor etching (CVE) of B_2O_3 by HF was experimentally monitored using Fourier transform infrared (FTIR) spectroscopy and quadrupole mass spectrometry (QMS). The spontaneous etching of B_2O_3 by HF gas was also analyzed using density functional theory (DFT). B_2O_3 films were grown using B_2O_3 atomic layer deposition with BCl_3 and H_2O as the reactants at 40 °C. FTIR spectroscopy then observed the CVE of B_2O_3 by HF at 150 °C. B_2O_3 etching was monitored by the loss of absorbance for B–O stretching vibration in B_2O_3 films. FTIR spectroscopy studies also observed B–F stretching vibrations from BF_x species on the B_2O_3 surface after HF exposures. In addition, the QMS analysis was able to identify the etch products during the spontaneous etching of B_2O_3 by HF gas at 150 °C. The QMS studies observed the main volatile etch products as BF_3, $BF_2(OH)$, and H_2O. Additional volatile etch products were also detected including $B_3O_3F_3$ and other boroxine ring compounds. The DFT predictions were consistent with the spontaneous etching of B_2O_3 by HF gas. DFT confirmed that CVE was likely because the energetics of the spontaneous etching reaction $B_2O_3(s) + 6HF(g) \rightarrow 2BF_3(g) + 3H_2O(g)$ were more favorable than the self-limiting reaction $B_2O_3(s) + 6HF(g) \rightarrow 2BF_3(s) + 3H_2O(g)$. The spontaneous etching of B_2O_3 was predicted at temperatures above −163 °C for an HF reactant pressure of 0.2 Torr and BF_3 and H_2O product pressure of 0.01 Torr.

I. INTRODUCTION

Etching has been important in making images and patterns for many centuries.[1] Dry etching has been particularly crucial in semiconductor processing.[2] The fabrication of three-dimensional device structures uses successive steps of deposition and etching in the presence of masks to control the areas for deposition and etching. Much of the previous dry etching has been performed using reactive radical and ionic species from plasmas.[3] Some dry etching has also utilized plasmaless thermal chemistry.[4,5] A prominent application of dry etching using only thermal chemistry is micromachining and feature release during MEMS processing.[6–8]

Compared with plasma etching, there are not many examples of dry thermal etching. The main demonstrations of dry thermal etching involve the formation of volatile halides using various halogenation reactants. For example, the dry thermal etching of silicon can occur spontaneously using XeF_2, F_2, or ClF_3 as the reactants.[4,5,9] Many metals can also be etched by exposure to halogenation reactants. Tungsten and niobium can undergo dry thermal etching using XeF_2.[7,8,10,11] Other metals, such as copper and aluminum, can also be spontaneously etched by Cl_2.[11,12]

Many metal oxides can also be spontaneously etched using ligand addition or halogenation reactions. Copper oxide, iron oxide, and other metal oxides can be spontaneously etched by exposure to ligands that can coordinate with the metal and produce volatile products.[13–15] The dry etching of SiO_2 can also occur with hydrogen fluoride (HF) in the presence of H_2O vapor at H_2O

pressures sufficient to form an H_2O multilayer on the SiO_2 surface.[16] Other examples of dry thermal spontaneous etching involve a variety of ligand-exchange reactions between metal fluorides and precursors that transfer ligands and volatilize the metal fluoride.[17–22]

Spontaneous etching is also involved in thermal atomic layer etching (ALE).[19,23] Two sequential reactions typically define thermal ALE. One reaction modifies the surface layer of the material and the second reaction leads to the volatile release of this modified surface layer.[19] For example, the surface modification of metal oxides and metal nitrides during thermal ALE can be performed using fluorination to form a metal fluoride.[19,24] The metal fluoride can then be volatilized using ligand-exchange reactions. Other mechanisms for thermal ALE can employ oxidation reactions to change the oxidation state of the metal or conversion reactions to convert the initial metal oxide to a different metal oxide that has an etching pathway.[19,25,26] If at least one reaction in the thermal ALE reaction sequence is self-limiting (SL), the other reactions in the sequence may involve spontaneous etching.

Spontaneous etching in thermal ALE reaction sequences has been identified in several systems. WO_3 ALE using BCl_3 and HF as the reactants involves the conversion of WO_3 to boron oxide (B_2O_3) and then the spontaneous etching of B_2O_3 by HF.[26] TiN ALE using O_3 and HF as the reactants is defined by the oxidation of TiN to TiO_2 and then the spontaneous etching of TiO_2 by HF.[27] In addition, Al_2O_3 ALE using HF and TMA as the reactants proceeds with the fluorination of Al_2O_3 to AlF_3 and then the spontaneous etching of AlF_3 by TMA.[18,27] In these examples, the conversion, oxidation, or fluorination reactions are self-limiting, and then the removal of the modified surface layer occurs by spontaneous etching.

The reaction of HF plays a pivotal role in many thermal ALE systems.[28,29] HF can fluorinate the initial material leading to the formation of a stable SL metal fluoride. Alternatively, HF can fluorinate and remove the initial material as a volatile fluoride by chemical vapor etching (CVE). The SL or CVE pathways are determined by the energetics and volatility of the reaction products. Having a better knowledge of HF reactions with metals and metal oxides will help improve the understanding of spontaneous etching and its role in thermal ALE.

In this article, the spontaneous etching of B_2O_3 by HF gas is examined using Fourier transform infrared (FTIR) spectroscopy, quadrupole mass spectrometry (QMS), and density functional theory (DFT). The FTIR analysis confirms the spontaneous etching of B_2O_3 by HF gas and reveals the species remaining on the B_2O_3 surface after HF etching. The QMS measurements identify the volatile etch products that leave the B_2O_3 surface during etching. The DFT investigations examine the energetics of the CVE and SL reactions between B_2O_3 and HF gas and predict the expected etch products versus temperature and reactant and product pressures.

II. EXPERIMENT AND METHODS

A. FTIR spectroscopy

The FTIR spectroscopy studies of B_2O_3 etching by HF were performed in a reactor reported previously.[30] Prior to B_2O_3 etching, the boron oxide was deposited using B_2O_3 atomic layer deposition (ALD) using sequential exposures of BCl_3 (≥99.9% trace metals basis, Sigma-Aldrich) and de-ionized H_2O at 35 °C.[26] The BCl_3 reaction was a 2 s exposure, followed by a 90 s purge. The FTIR scan was then recorded for 60 s. The water reaction consisted of a 1 s exposure, followed by a 60 s purge. The FTIR scan was then again recorded for 60 s.

The B_2O_3 ALD film was deposited on silicon nanoparticles (>98% U.S. Research Nanomaterials). The silicon nanoparticles had a diameter of ~30–50 nm. The silicon nanoparticles have a large surface area and ensure a high signal-to-noise ratio when using transmission FTIR spectroscopy to identify surface species.[25] The silicon nanoparticles were pressed into a tungsten grid. The FTIR spectroscopy was then conducted by passing the IR light through the tungsten grid.[31] The tungsten grid was $\sim 1.7 \times 3.0\ cm^2$, 50 μm thick with 100 grid lines per inch. The tungsten grid was resistively heated with a DC power supply (6268B, 12 V/40 A, HP). The power supply was controlled by a PID temperature controller (Love Controls 16B, Dwyer Instruments). To monitor the temperature, a type K thermocouple was connected to the tungsten grid with a nonconductive epoxy (Cermabond 571).

The B_2O_3 spontaneous etching experiments were performed using HF-pyridine (70 wt. % HF, Sigma-Aldrich) as the HF source.[32] Each HF exposure was a 2 s static exposure of HF at 200 mTorr followed by a 90 s purge. Subsequently, the FTIR scan was recorded for 60 s. Longer purges than necessary were used to eliminate the possibility of HF contact with the KBr windows during the FTIR scan.

B. Quadrupole mass spectroscopy

The QMS investigations employed a new reactor that has been described earlier.[22] This reactor is different from a previous reactor that employed static exposures and then sampled the gas-phase products using a pulsed valve.[33] The new reactor studies volatile etch products produced by flowing reactant gases through powder samples. The volatile etch products and background gas were expanded through an aperture to form a molecular beam. The beam of background gas and volatile etch products were then passed through a skimmer and entered a differentially pumped region for the QMS analysis.

The skimmer aperture diameter was 1.4 mm and the skimmer was positioned 41 mm from the sample aperture.[22] The volatile etch products were observed using a high sensitivity, high mass quadrupole mass spectrometer (Extrel, MAX-QMS Flange Mounted System). Each spectrum monitored mass intensities from 2 to 300 amu and was recorded in 1 s. An average of 100 scans was collected during HF exposures to help eliminate noise. Electron-impact ionization of gas-phase etching products was achieved with a circular thoriated iridium filament in the ionization volume inside the ionizer housing. An electron ionization energy of 70 eV was used for these experiments.

HF was first introduced into a reservoir at a pressure of 9 Torr to have a consistent HF partial pressure during the reaction. HF was leaked into the flowing N_2 background gas. The HF pressure in the sample holder containing the B_2O_3 powder was 5.2 Torr. The background N_2 pressure was 2.8 Torr. B_2O_3 nanopowder was purchased from U.S. Research Nanomaterials (99.9%, 165 nm

diameter) and added to the sample holder. The mass of the B_2O_3 nanopowder was recorded before and after the etching experiments. The mass of the B_2O_3 nanopowder before spontaneous etching was 50.5 mg.

C. Density functional theory

The computational approach is similar to the approach employed in previous studies.[28,29] In these earlier investigations, the energetics and thermochemistry of SL and CVE reactions were compared to reveal their competition. In the CVE reaction, the HF precursor gas molecules etch B_2O_3 and form gaseous products. In the SL reaction, the HF precursor gas molecules interact and passivate the material surface by forming a nonvolatile fluoride layer.

This computational study considered the following CVE and SL reactions:

$$\text{CVE1:} B_2O_{3(b)} + 6\,HF_{(g)} \rightarrow 2\,BF_{3(g)} + 3\,H_2O_{(g)}, \quad (1)$$

$$\text{CVE2:} 4\,B_2O_{3(b)} + 14\,HF_{(g)} \rightarrow 5\,H_2O_{(g)} + BF_{3(g)} + 4\,B(OH)F_{2(g)} + B_3O_3F_{3(g)}, \quad (2)$$

$$\text{SL:} 2\,B_2O_3^* + 12\,HF_{(g)} \rightarrow 4\,BF_3^* + 6\,H_2O_{(g)}. \quad (3)$$

In these reactions, b indicates bulk, g refers to gas, and the asterisks designate surface species. These are overall reactions for spontaneous etching (CVE1 and CVE2) or surface fluorination (SL) of B_2O_3. These reactions are independent of the reaction pathway. Reaction kinetics are not considered in this study.

This computational approach revealed that there is a "minimum thermodynamic barrier" that must be overcome to allow etching from the passivated surface. Based on the value of this "minimum thermodynamic barrier" and the respective energies of the CVE and SL reactions, the HF precursor gas pulse can be in one of the four following states: purely self-limiting, preferred self-limiting, preferred etching, and purely etching. These states are discussed in detail in previous studies.[28]

All the DFT calculations performed in this study were based on the spin-polarized generalized gradient approximation using the Perdew–Burke–Ernzerhof (PBE) exchange-correlation (XC) functional[34] as implemented in the Vienna *ab initio* simulation package (VASP).[35] In this approach, the valence electrons are treated explicitly by expanding their wave functions in a plane wave basis up to an energy cutoff of 400 eV, whereas the core electrons are treated by projector augmented waves.[36,37]

The enthalpy and entropy contributions of the bulk and surface geometries were computed with the help of the PHONOPY code,[38] which requires accurate interatomic force constants obtained from density functional perturbation theory (DFPT) calculations in VASP. The total electronic energies of gas-phase molecules, BF_3 and H_2O, were computed in VASP by placing the molecules in a large periodic box of dimensions $15.0 \times 15.5 \times 16.0$ Å^3 and relaxing their geometries. However, the enthalpy and entropy contributions of the gas-phase molecules were obtained from the free enthalpy (freeh) code of Turbomole suite[39] using the PBE XC functional and triple zeta basis set (def-TZVPP).

To model the bulk B_2O_3 geometry, a trigonal lattice geometry was employed from the materials project database.[40] The geometry is simultaneously reoptimized for the ionic positions, cell shape, and cell volume with an increased plane wave energy cutoff of 550 eV and a Monkhorst–Pack K-point mesh of $4 \times 4 \times 2$. The converged lattice parameters were found to be $a = b = 4.4027$ Å, $c = 8.8174$ Å, $\alpha = \beta = 90°$, and $\gamma = 120°$ as shown in Fig. 1(a).

A 9.4 Å thick slab of trigonal B_2O_3 sliced along the (1 0 1) surface plane with 15 Å of vacuum separating the periodic images along the surface normal was then chosen to represent the surface model for the self-limiting reaction. This surface slab model consisted of three layers of 6 B_2O_3 units ($B_{36}O_{54}$) as shown in Fig. 1(b). To model the fluorinated surface, six surface O atoms were removed as H_2O and 12 F atoms were introduced such that the F atoms bind to surface boron atoms as shown in Fig. 1(c). The geometry was optimized to obtain the ground state electronic energy. Only the top most layer of these surfaces was considered for the DFPT calculations.

The reaction free energy (ΔG) discussed in this article was computed as

$$\Delta G = \Delta H\text{-}T\Delta S + RTln(Q), \quad (4)$$

where

$$\Delta H = \Delta E + \Delta ZPE + \Delta W(T), \quad (5)$$

$$Q = \Pi p^{\mu}_{products} / \Pi p^{\mu}_{reactants}. \quad (6)$$

In these equations, ΔH and ΔS are the enthalpy and entropy change, respectively. ΔH is computed as the sum of the electronic reaction energy (ΔE), zero point energy change (ΔZPE), and a temperature-dependent contribution [W(T)]. R is the gas constant, Q is the reaction quotient that allows for changes in reactant and product pressures, and μ is the stoichiometric coefficient of the respective reactant and product species.

III. RESULTS AND DISCUSSION

A. FTIR spectroscopy

The etching of B_2O_3 films was studied using transmission FTIR spectroscopy. To study the etching of B_2O_3 films, B_2O_3 was first deposited on silicon nanoparticles. FTIR studies of B_2O_3 ALD are shown in Fig. 2. B_2O_3 ALD was performed with BCl_3 and H_2O as the reactants at a low deposition temperature of ~40 °C.[26] The overall reaction is $2BCl_3 + 3H_2O \rightarrow B_2O_3 + 6HCl$. The BCl_3 exposure was conducted for 1 s at 500 mTorr. The H_2O exposure was conducted for 1 s at 80 mTorr. B_2O_3 ALD with BCl_3 and H_2O is similar to B_2O_3 ALD using BBr_3 and H_2O.[41] Earlier studies of B_2O_3 ALD films using BCl_3 and H_2O have been performed and found to have the correct B_2O_3 stoichiometry by XPS.[26]

Figure 2 shows the FTIR spectra referenced to the original silicon nanoparticle substrate. After the first BCl_3 and H_2O cycle, absorbance gains are measured at 1450 and 1315 cm^{-1} and a smaller absorbance loss is observed at 1250 cm^{-1}. These absorbance features can be identified as a gain of B–O stretching vibrations

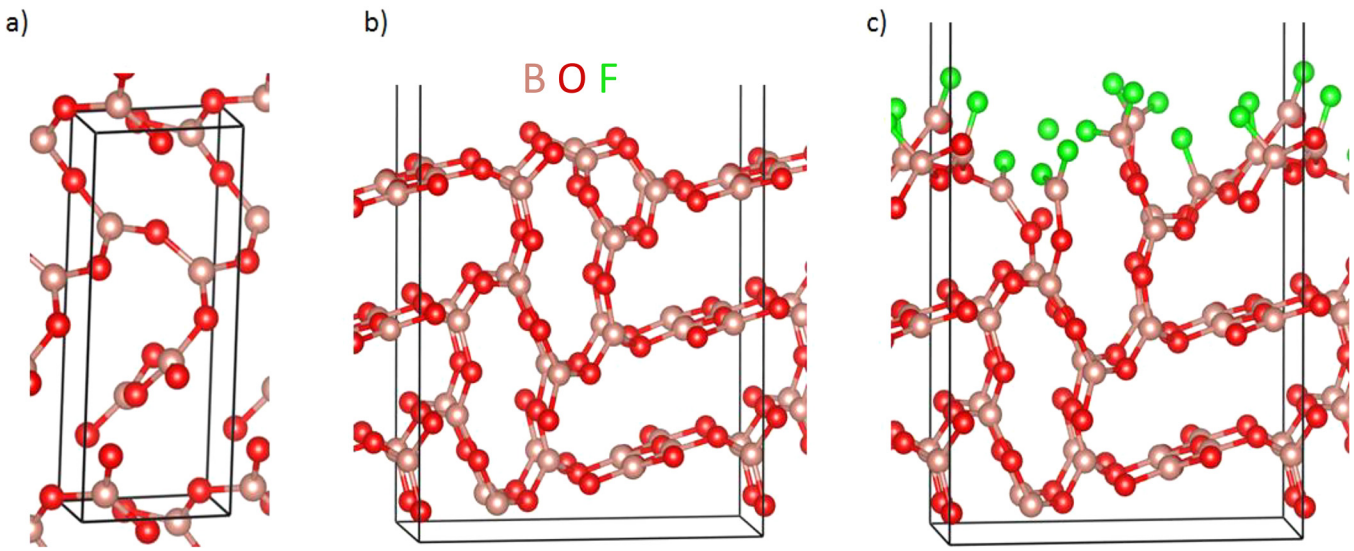

FIG. 1. (a) Reoptimized trigonal lattice geometry for B_2O_3 bulk. (b) Bare (1 0 1) surface of trigonal B_2O_3. (c) Fluorinated B_2O_3 surface from (b) after removing six surface O atoms.

and a small loss of Si–O–Si vibrations, respectively.[42–45] The loss of absorbance for Si–O–Si vibrations likely results from boron being slightly soluble in silicon.[46] Three main vibrational modes grow at 1450, 1315, and 730 cm^{-1} with an increasing number of B_2O_3 ALD cycles up to 15 cycles. These vibrational features are assigned to different boron-oxygen stretching modes and ring-stretching modes in boric acid and borate.[42,43,45,47]

Difference spectra recorded during the 13th BCl_3 and H_2O exposures during B_2O_3 ALD are displayed in Fig. 3. These difference spectra are consistent with the sequential AB reactions during B_2O_3 ALD as

$$(A)\ BOH^* + BCl_3(g) \rightarrow BOBCl_2^* + HCl(g), \quad (7)$$

$$(B)BCl^* + H_2O(g) \rightarrow BOH^* + HCl(g). \quad (8)$$

In these equations, the asterisks indicate the surface species.

In Fig. 3(a), positive vibrational absorbance peaks are observed at 1530, 1362, 1273, and 950 cm^{-1} after the BCl_3 exposure. The

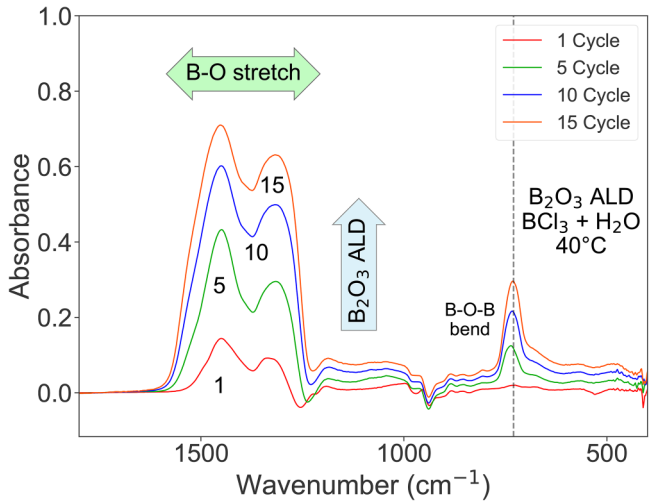

FIG. 2. Infrared absorbance spectra from 400 to 1800 cm^{-1} during B_2O_3 ALD using BCl_3 and H_2O as reactants after 1, 5, 10, and 15 B_2O_3 ALD cycles at 40 °C.

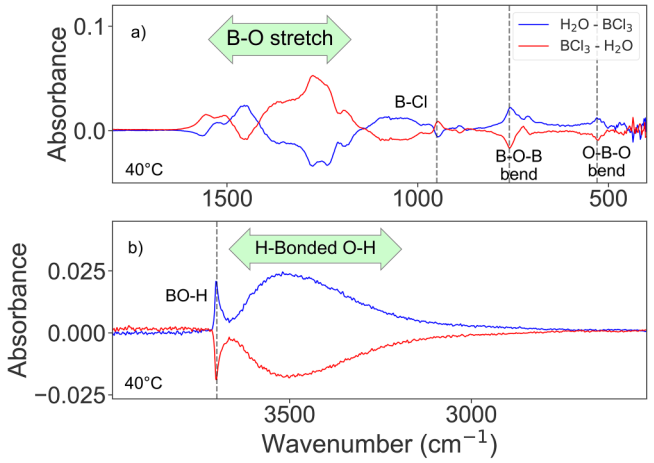

FIG. 3. Infrared difference spectra recorded after BCl_3 and H_2O exposures during 13th B_2O_3 ALD cycle at 40 °C. (a) Difference spectra between 400 and 1800 cm^{-1}. (b) Difference spectra between 2500 and 4000 cm^{-1}.

absorbance peaks at 1530, 1362, and 1273 cm^{-1} are attributed to different boron oxide vibrations such as ring-stretching boroxol vibrations and B–O stretching vibrations.[42,43,45,47] The absorbance peak at 950 cm^{-1} is attributed to B–Cl surface vibrations left on the surface after BCl_3 exposure.[48] There may also be B–Cl vibrations found between 1300 and 1500 cm^{-1} that are largely obscured by the absorbance from B–O vibrational modes.[48] Negative vibrational absorbance peaks are also observed at 750 and 500 cm^{-1} after BCl_3 exposure. These peaks are assigned to BO_2 bending vibrations.[42,45,47] A small loss at 1450 cm^{-1} is assigned to B–OH and is likely lost resulting from the BCl_3 reaction with BOH species.[43]

Positive vibrational absorbance peaks are also observed in Fig. 3(a) at 1440, 730, and 530 cm^{-1} after the H_2O exposure. These vibrational features result from the reaction of H_2O with BCl surface species. These are likely B–OH stretching vibrations and the bending modes of BO_2.[45] In addition, there are also negative absorbance peaks at 1530, 1362, 1273, and 950 cm^{-1} after the H_2O exposure. These negative absorbance peaks after the H_2O exposure mirror the reverse of the positive absorbance peaks monitored after the BCl_3 exposure.

Figure 3(b) shows the change in the O–H stretching vibrations after H_2O and BCl_3 exposures. After H_2O exposures, there is an increase at 3700 cm^{-1} that is consistent with isolated O–H groups in boric acidlike films.[49] There is also a very broad peak at 3600–3000 cm^{-1} that is attributed to hydrogen-bonded BOH species on the surface.[49] The positive absorbance features observed after the H_2O exposure are then almost exactly reversed when the BOH species are removed from the surface by reaction with the BCl_3 exposure.

The spontaneous etching of B_2O_3 by HF gas was then examined using the B_2O_3 ALD films. FTIR spectra were recorded after each 2 s static exposure of HF at 200 mTorr at 150 °C. These FTIR spectra were referenced to the initial B_2O_3 ALD film on the silicon nanoparticles. The progressive FTIR spectra versus number of HF exposures for nine HF exposures on B_2O_3 are shown in Fig. 4. Each consecutive HF exposure removes a fraction of the absorbance from the B_2O_3 ALD film. This absorbance loss corresponds to CVE of the B_2O_3 film. The vibrational modes at 1450, 1315, and 730 cm^{-1} are attributed to B–O vibrations as discussed earlier during the growth of the B_2O_3 ALD films.[42,43,45,47]

The first HF exposure in Fig. 4 only removes a small fraction of the B_2O_3 film. Perhaps the first HF exposure is required to fluorinate the surface and condition the B_2O_3 film. The largest absorbance losses are observed during the second, third, and fourth HF exposures in Fig. 4. The absorbance losses are reduced during the subsequent HF exposures. By the eighth HF exposure, the B_2O_3 film has been completely removed by the CVE reaction.

The spontaneous etching of B_2O_3 by HF at 150 °C is consistent with earlier results for B_2O_3 etching by HF at 207 °C observed by spectroscopic ellipsometry studies.[26] These previous studies were conducted to confirm that HF could spontaneously remove B_2O_3 films after using BCl_3 to convert the surface of WO_3 to a B_2O_3 layer. The conversion of WO_3 to B_2O_3 was an important step in the thermal ALE of WO_3 using BCl_3 and HF and also the thermal ALE of W using O_2/O_3, BCl_3 and HF.[26]

The earlier study of WO_3 ALE examined B_2O_3 ALD films grown using BCl_3 and H_2O as the reactants and then etched the B_2O_3 ALD films using HF exposures of 100 mTorr s.[26] Each HF exposure removed ≈1.8 Å of B_2O_3 at 207 °C.[26] In contrast, approximately 5 HF exposures were required to remove the B_2O_3 ALD film in Fig. 4 where each HF exposure was 400 mTorr s. Based on a B_2O_3 ALD growth rate of ≈1 Å/cycle using BCl_3 and H_2O,[26] the etch rate in Fig. 4 for the B_2O_3 film grown using 15 B_2O_3 ALD cycles is ≈3 Å/HF exposure. There is reasonable agreement between these etch rates per HF exposure given the different HF exposures and temperatures.

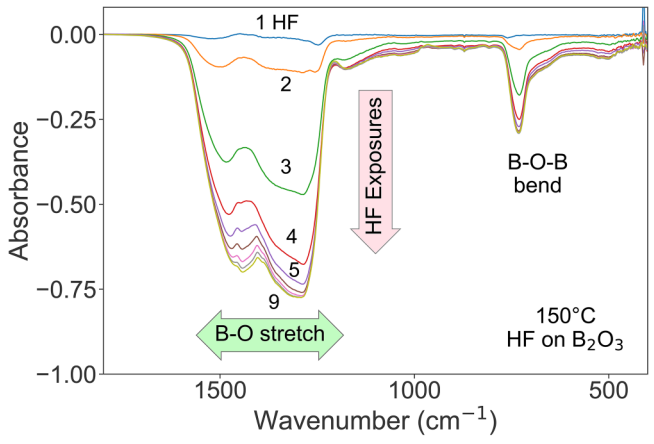

FIG. 4. Infrared difference spectra between 400 and 1800 cm^{-1} recorded after consecutive HF exposures on the B_2O_3 ALD film at 150 °C using the original B_2O_3 ALD film as reference. Original B_2O_3 ALD film is nearly completely removed after >5 HF exposures.

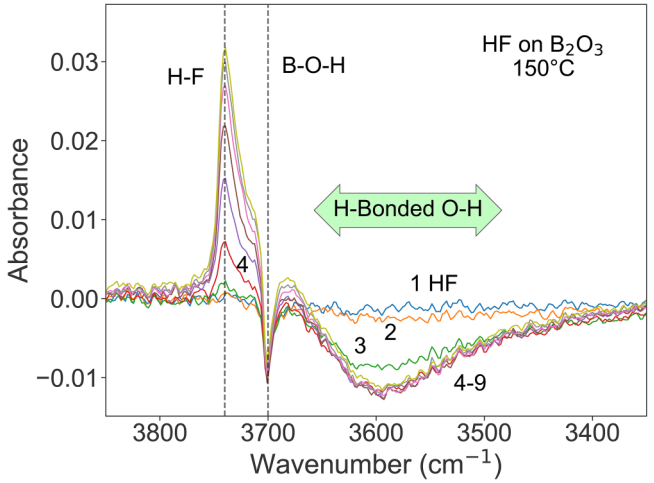

FIG. 5. Infrared difference spectra between 3350 and 3850 cm^{-1} recorded after consecutive HF exposures on the B_2O_3 ALD film at 150 °C using the original B_2O_3 ALD film as reference.

Figure 5 shows difference spectra from 3350 to 3850 cm^{-1} referenced to the initial B_2O_3 film during HF exposures on B_2O_3. There is an absorbance increase at 3740 cm^{-1}, an absorbance loss at 3700 cm^{-1}, and another broad absorbance loss from 3400 to 3700 cm^{-1}. The positive absorbance feature at 3740 cm^{-1} appears after the fourth HF exposure and is attributed to H–F stretching vibrations from adsorbed HF on the surface.[50,51] Figure 4 shows that most of the B_2O_3 film has been etched by the fourth HF exposure. Before the fourth HF exposure, HF was presumably consumed by the B_2O_3 etching reaction.

Figure 5 shows that the peak at 3700 cm^{-1} decreases and is constant after the first HF exposure. This peak is attributed to terminal BO–H vibrational stretching vibrations.[49] Terminal BOH species were also present during B_2O_3 ALD after the H_2O exposure as shown in Fig. 3(b). These terminal BOH species are consumed by the first HF exposure. The broad absorbance loss from 3400 to 3700 cm^{-1} is also assigned to the loss of hydrogen-bonded BOH groups on the B_2O_3 film.[49] However, these hydrogen-bonded BOH groups are not removed until after the fourth HF exposure. The removal of these hydrogen-bonded BOH groups coincides with the growth of absorbance assigned to HF on the B_2O_3 surface.

Figure 6 shows the FTIR difference spectra during the first HF exposure and during the last (ninth) HF exposure. The first HF exposure is referenced to the initial B_2O_3 ALD film and the ninth HF exposure is referenced to the eighth HF exposure to understand the change of each individual HF exposure. For comparison, these difference spectra are contrasted with the inverted absorbance for the B_2O_3 ALD film over the same frequency range. The FTIR difference spectrum after the first HF exposure shows apparent absorbance loss peaks at 1242 and 1517 cm^{-1}. These two apparent absorbance loss peaks result from removal of B–O vibrations together with an absorbance gain at 1440 cm^{-1} resulting from another vibrational feature. The absorbance gain at 1440 cm^{-1} does not appear as a positive absorbance peak because this absorbance gain occurs concurrently with a larger absorbance loss resulting from B_2O_3 spontaneous etching.

If the first HF exposure was only removing B_2O_3, then the FTIR difference spectra after the first HF exposure and the absorbance from the B_2O_3 ALD film should be similar in Fig. 6. The discrepancy between the first HF exposure and ninth HF exposure can be explained by the growth of absorbance from B–F vibrational modes of BF_x surface species at 1440 cm^{-1}.[52–55] This new positive absorbance partially offsets the absorbance loss resulting from B_2O_3 etching. Subsequent HF exposures lead to the loss of more B_2O_3 and the comparison between the FTIR difference spectra and the absorbance from the B_2O_3 ALD film is more similar as shown in Fig. 4. This behavior is expected if the BF_x surface species stay constant during subsequent HF exposures while the B–O absorbance losses continue to increase with more HF exposures.

Further confirmation for the assignment of B–F stretching vibrations from BF_x surface species centered at ~1430 cm^{-1} is derived from the evolution of the difference spectra with each HF exposure. The FTIR difference spectra after the ninth exposure show only an absorbance loss centered at 1430 cm^{-1}. This absorbance loss is again consistent with the B–F stretching vibrations from BF_3 surface species.[52–55] In this case, nearly all the B_2O_3 has been etched away. The ninth HF exposure then removes the last of the B–F surface species.

The B_2O_3 was also easily etched by HF at lower temperatures than 150 °C. Figure 7 shows the etching of B_2O_3 during HF exposures at a lower temperature of 40 °C. This temperature was the lowest temperature examined in this study. The B–O vibrational feature at 1200–1600 cm^{-1} decreases in intensity during the first and second HF exposures. The absorbance loss is faster than the

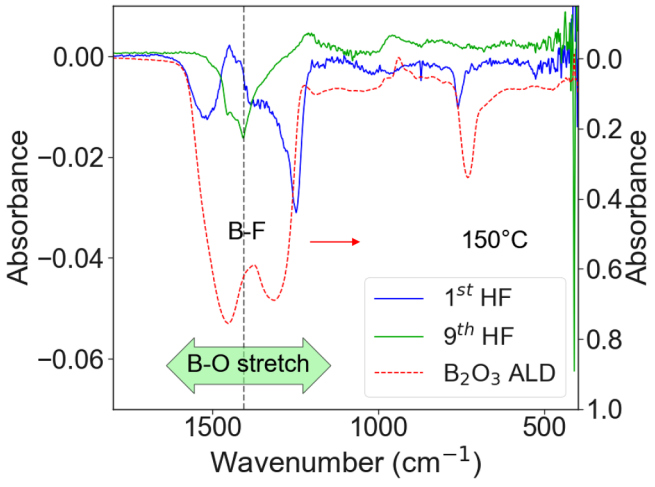

FIG. 6. Infrared difference spectra showing absorbance after first HF exposure referenced to the initial B_2O_3 ALD film and ninth HF exposure referenced to absorbance after the eighth HF exposure. Inverted absorbance for original B_2O_3 ALD film is also shown for comparison.

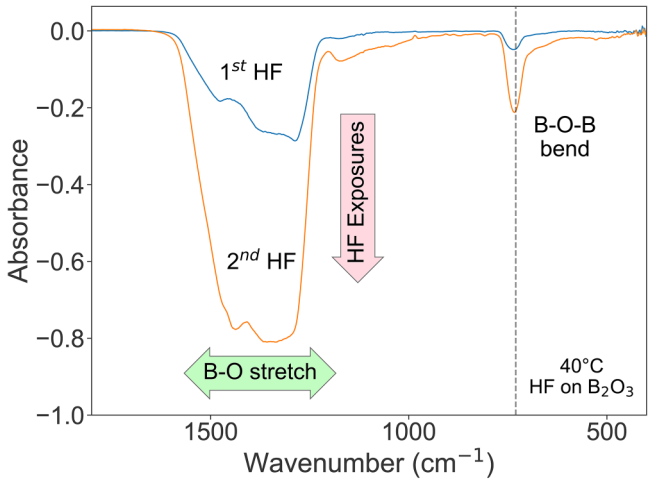

FIG. 7. Infrared difference spectra between 400 and 1800 cm^{-1} recorded after consecutive HF exposures on B_2O_3 ALD film at 40 °C using the original B_2O_3 ALD film as reference. Original B_2O_3 ALD film is nearly completely removed after 2 HF exposures.

absorbance loss observed for B_2O_3 etching at 150 °C as shown in Fig. 4. However, the B_2O_3 etching rate was not quantified versus temperature.

B. Quadrupole mass spectrometry

QMS was used to identify the volatile etch products during the spontaneous etching of B_2O_3 by HF. The QMS observed that the main volatile etch products were BF_3, $BF_2(OH)$, and H_2O. Figure 8 shows a portion of the mass spectrum from 40 to 70 amu during the first and fifth HF exposures at 150 °C on B_2O_3. In this spectral range, the main peaks are assigned to BF_3 and $BF_2(OH)$. The largest masses at $m/z = 68$ and 67 amu are assigned to the BF_3^+ molecular ion. The shapes of the clusters are determined by the 80:20 isotopic ratio between ^{11}B and ^{10}B. The ratio of the signal intensities at $m/z = 68$ and 67 amu is consistent with the natural isotopic abundance of boron.

The largest mass intensity is observed for a fragment of BF_3^+ corresponding to BF_2^+ at $m/z = 49$ amu for ^{11}B. There is also a signal at $m/z = 48$ amu based on the isotopic abundance of ^{10}B. This peak also has the correct signal intensity relative to the signal at $m/z = 49$ amu. In addition, there are other peaks at $m/z = 66$ and 65 amu that are assigned to $BF_2(OH)$. The fragmentation of $BF_2(OH)^+$ also produces a signal for $BF(OH)^+$ at $m/z = 47$ and 46 amu. The species $BF_2(OH)^+$ and $BF(OH)^+$ have been observed and characterized previously by reacting BF_3 with $B(OH)_3$ at room temperature.[56] The etching of B_2O_3 can also be confirmed by the mass loss of B_2O_3 powder. The initial mass of the B_2O_3 powder was 50.5 mg. After multiple HF exposures, the B_2O_3 powder mass was reduced to 24.8 mg.

Figure 8(a) shows that there are more $BF_2(OH)$ species observed during the first HF exposure compared with the fifth HF exposure displayed in Fig. 8(b). In particular, the signals for $BF_2(OH)^+$ and $BF(OH)^+$ both drop dramatically versus the signal for BF_2^+ when comparing Figs. 8(a) and 8(b). The initial B_2O_3 powder was loaded into the chamber from ambient air. The air exposure likely hydrated the B_2O_3 surface to form a boric acidlike surface. This surface yields more OH species during HF etching.

Figure 9 shows the mass signals at higher mass from $m/z = 75$ to 140 amu. This portion of the mass spectrum corresponds to boroxine ring compounds. The existence of gas-phase $B_3O_3F_3$ boroxine rings has been previously reported and characterized using mass spectrometry.[57] Figure 9 reveals that clusters of mass peaks are observed around $m/z = 136$, 118, 92, and 79 amu. The peaks located from $m/z = 131$ to 140 amu are shown on an expanded scale in Fig. 10. These peaks are attributed to the parent $B_3O_3F_3$, $B_3O_3F_2OH$, and $B_3O_3F(OH)_2$ boroxine rings. The identity of these peaks is confirmed by the predictions for their masses based on the isotopic abundance of ^{11}B and ^{10}B shown in Fig. 10.

The next grouping of peaks is observed around $m/z = 118$ amu in Fig. 9. These peaks are consistent with $B_3O_3F_2^+$ and $B_3O_3F(OH)^+$. These peaks are assigned to fragments of the $B_3O_3F_3$ and $B_3O_3F_2OH$ boroxine ring compounds. The grouping of peaks around $m/z = 92$ amu is attributed to $B_2OF_2OH^+$ and $B_2OF_3^+$ and assigned to boron dimers or fragments of the parent boroxine rings. Likewise, the grouping of peaks around $m/z = 79$ amu is attributed to $B_2F_3^+$ and $B_2F_2(OH)^+$ and assigned to boron dimers or fragments. The signals for the boroxine rings with hydroxyl groups in Fig. 9 are much larger during the first HF exposure compared with the fifth HF exposure. The larger hydroxyl content during the first HF exposure is again attributed to the initial boric acidlike surface of the B_2O_3 powders. This hydrated B_2O_3 surface is removed by the fifth HF exposure.

The etch products evolve versus the number of HF exposures on the B_2O_3 powder. Figure 11 shows the evolution of the main volatile etch products during the first five HF exposures on the

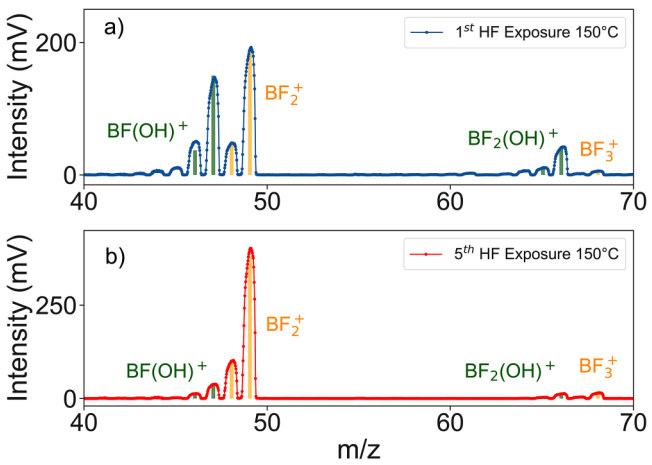

FIG. 8. Mass spectrum of products monitored in the range of $m/z = 40$–75 amu during spontaneous etching of B_2O_3 by HF at 150 °C during the (a) first HF exposure and (b) fifth HF exposure. Observed products are BF_3 and $B(OH)F_2$.

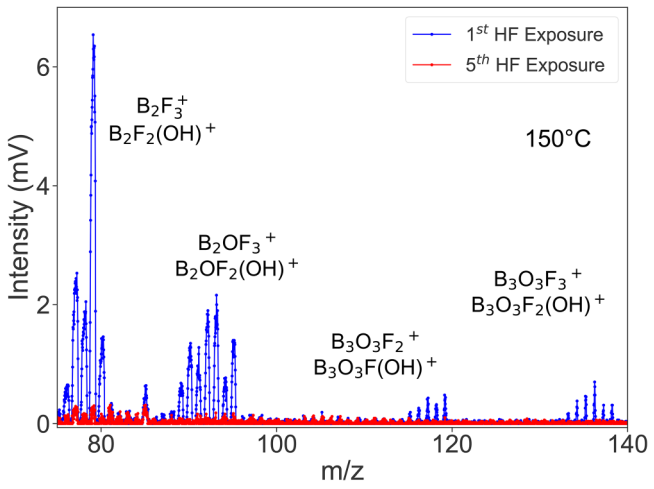

FIG. 9. Mass spectrum of products monitored in the range of $m/z = 70$–140 amu during spontaneous etching of B_2O_3 by HF at 150 °C during the (a) first HF exposure and (b) fifth HF exposure. Observed products are $B_3O_3F_3$, $B_3O_3F_2OH$, and $B_3O_3F(OH)_2$ boroxine rings.

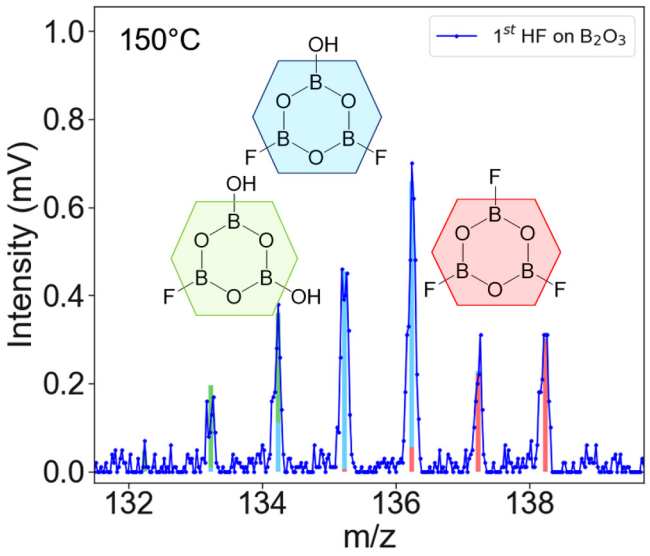

FIG. 10. Mass spectrum of products monitored in the range of $m/z = 131–140$ amu during spontaneous etching of B_2O_3 by HF at 150 °C. Parent peaks of $B_3O_3F_3$, $B_3O_3F_2(OH)$, and $B_3O_3F(OH)_2$ boroxine rings are observed during the first HF exposure.

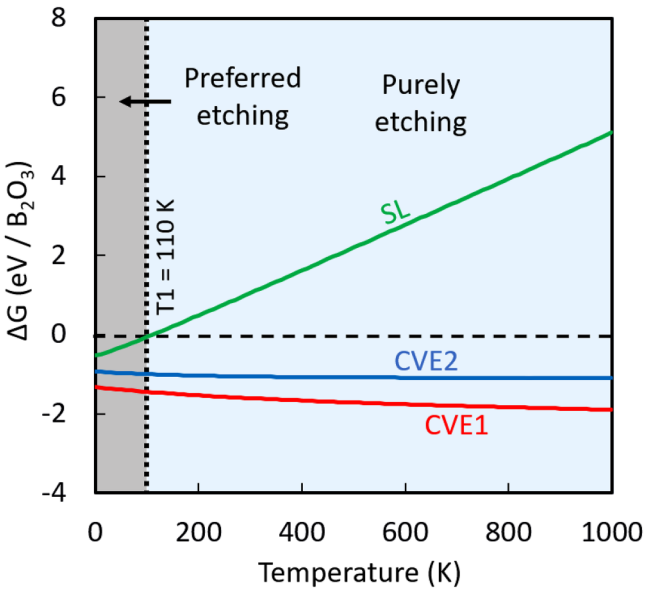

FIG. 12. ΔG free energy profiles of CVE1, CVE2, and SL reactions vs temperature at a constant HF reactant pressure of 0.2 Torr and a product pressure of 0.01 Torr. SL reaction becomes endergonic at 110 K.

B_2O_3 powder. Figure 11(a) shows the mass intensities for BF_2^+ and $BF(OH)^+$. These species are the highest mass intensities corresponding to BF_3 and $BF_2(OH)$ volatile etch products. Figure 11(b) displays the mass intensities for H_2O^+ corresponding to the same first five HF exposures.

A comparison between the signals for BF_2^+ and $BF(OH)^+$ for the first five HF exposures in Fig. 11(a) reveals that the intensity for the $BF(OH)^+$ drops significantly with increasing HF exposures. In contrast, the intensity for H_2O^+ in Fig. 11(b) is very constant for the second to fifth HF exposures. The decrease in the signal for $BF(OH)^+$ is consistent with HF etching through the initial surface of the hydrated B_2O_3 powder. After removing this boric acidlike surface of the B_2O_3 powder, the HF exposure yields primarily BF_3 as the volatile etch product.

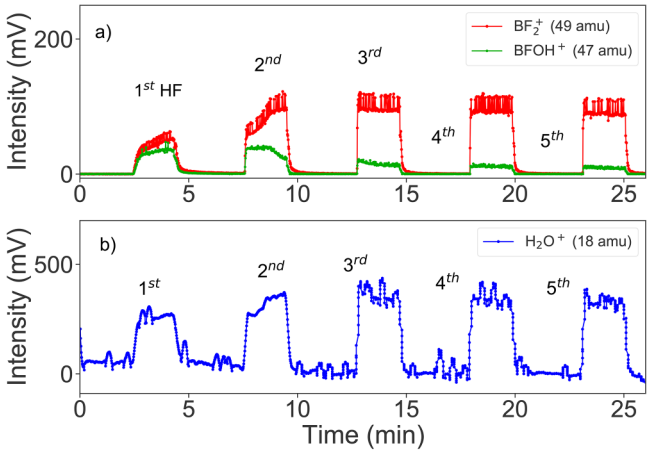

FIG. 11. Mass traces of (a) BF_2^+ at $m/z = 47$ amu and $BFOH^+$ at $m/z = 49$ amu and (b) H_2O^+ at $m/z = 18$ amu vs time during the first five HF exposures on B_2O_3 powder.

C. Density functional theory

DFT was used to determine the reaction energies and "minimum thermodynamic barriers" to etch. The CVE1 reaction is $B_2O_3 + 6\,HF(g) \rightarrow 2\,BF_3(g) + 3\,H_2O(g)$. This reaction needs 6 HF molecules to etch a unit bulk of B_2O_3 and form 2 BF_3 and 3 H_2O gas-phase molecules. The BF_3 and H_2O reaction products are consistent with the results from the QMS studies. The CVE1 reaction is determined to be exoergic with a reaction energy of −1.6 eV. The SL reaction is also exoergic with a reaction energy of −0.8 eV. This SL reaction energy is less exoergic than the CVE1 reaction by 0.8 eV. Consequently, the spontaneous etch reaction is more favorable than the self-limiting reaction, and there is a negative "minimum thermodynamic barrier" for spontaneous etching.

The CVE2 reaction is $4\,B_2O_3 + 14\,HF(g) \rightarrow 5\,H_2O(g) + BF_3(g) + 4\,B(OH)F_2(g) + B_3O_3F_3(g)$. This reaction was considered to study the formation of the $B(OH)F_2$ and $B_3O_3F_3$ reaction products. These reaction products were also identified by the QMS investigations. The CVE2 reaction is exoergic with a reaction energy of −1.1 eV. However, this reaction energy of −1.1 eV is only −0.27 eV per each B_2O_3 unit. Therefore, this reaction energy is much less than the reaction energy of −1.8 eV per each B_2O_3 unit

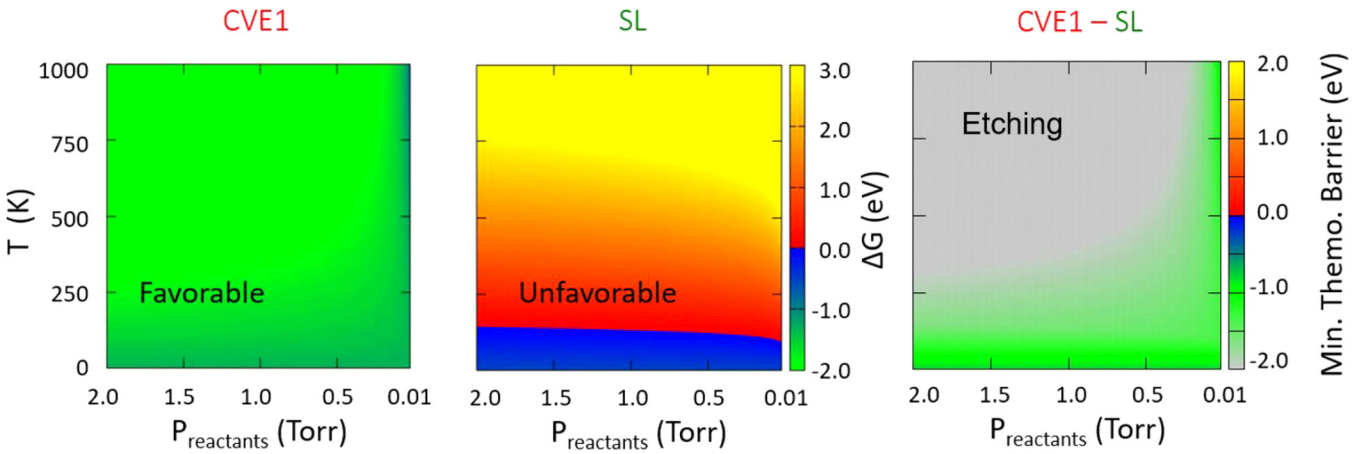

FIG. 13. 2D heat maps of ΔG free energies of CVE1 and SL reactions and corresponding "minimum thermodynamic barrier" to etch given by CVE1-SL at different reactant HF pressures from 0.01 to 2.0 Torr at a constant product pressure of 0.01 Torr. The CVE1 and SL contour plots (left and middle) share the same color bar and *y* axis.

for the CVE1 reaction. The "minimum thermodynamic barrier" to etch B_2O_3 and form these $B(OH)F_2$ and $B_3O_3F_3$ products is also negative. The much larger reaction energy for the CVE1 reaction is consistent with the QMS observation of primarily BF_3 etch products after removing the hydrated layer on the B_2O_3 powder.

Figure 12 displays the free energy profiles (FEPs) of CVE1, CVE2, and SL reactions in the temperature range of 0–1000 K at a constant HF reactant pressure of 0.2 Torr and a product pressure of 0.01 Torr. The SL reaction is exergonic at 0 K and increases in free energy with temperature. The SL reaction crosses the zero line at 110 K and becomes endergonic at higher temperatures. In comparison, the free energies of CVE1 and CVE2 reactions are exergonic at 0 K. The free energies of the CVE1 and CVE2 reactions decrease with temperature albeit with a small negative slope. The FEP of the CVE1 reaction has a comparatively slightly larger negative slope than the FEP of the CVE2 reaction. The CVE1 and CVE2 reactions never cross the zero line.

The region up to 110 K in Fig. 12 is labeled as "preferred etching" since the CVE reactions are more favorable than the SL reaction and both CVE and SL reactions are exergonic in this temperature range. The region at temperatures greater than 110 K in Fig. 12 is labeled as "purely etching." In this temperature zone, the SL reaction is endergonic. The stable surface B–F bonds at $T < 110$ K (−163 °C) are not favorable in the presence of a continuous supply of HF gas at $T > 110$ K. The experimental FTIR and QMS observations of spontaneous etching of B_2O_3 by HF exposure at 150 °C (423 K) are in the "purely etching" region and consistent with these computational results. The FTIR results of spontaneous B_2O_3 etching by HF at 40 °C and the earlier spectroscopic ellipsometry measurements of spontaneous B_2O_3 etching by HF at 207 °C are also in agreement with these theoretical predictions.[26]

The FEPs of the CVE1 and SL reactions were then examined at different reactant HF pressure from 0.01 to 2.0 Torr at a constant product pressure of 0.01 Torr in the temperature range of 0–1000 K. The resulting free energy changes for CVE1 and SL reactions and the difference between the reactions, CVE1-SL, are shown in Fig. 13. The CVE1 reaction is favorable at all pressures and temperatures. An increase in the reactant HF pressure decreases the slope of the CVE1 FEP and makes the reaction slightly more favorable at any given temperature. In agreement with Fig. 12, the SL reaction displays a zero crossing at approximately 110 K (−163 °C) at all pressures. The plot of CVE1-SL does not show significant change versus reactant pressure. The spontaneous etching reaction becomes only slightly more favorable relative to the self-limiting reaction as the reactant pressure increases.

The FEPs of the CVE1 and SL reactions were also explored at different product pressures of 0.01, 0.2, 1, and 2 Torr for reactant HF pressures from 0.01 to 2.0 Torr in the temperature range of 0–1000 K. The resulting free energy changes for CVE1 and SL reactions and the difference between the reactions, CVE1-SL, are displayed in Fig. 14. Note that the product pressure cannot be controlled in an etch reactor. These plots are thermochemical predictions at some chosen product pressures.

First, looking at the top row of contour plots in Fig. 14, the free energy of CVE1 increases with the increase in the product pressure and the reaction becomes unfavorable at high temperatures and low reactant pressures. This behavior is not surprising because a high product pressure and low reactant pressure indicates that the chamber is mostly filled with the product species. The forward reaction cannot be the most favorable. Second, looking at the middle row of plots in Fig. 14, the free energy of SL also increases with product pressure. The temperature for the zero crossing ($\Delta G = 0$) for the SL FEP also decreases, although with a very small change, at higher product pressures.

Third, the last row of plots in Fig. 14 shows the contour plot of the minimum thermodynamic barrier (CVE1-SL). Here, the colored region shows the pressure-temperature window for favorable etching. The unfavorability of both the CVE1 and SL reactions at high product pressure leads to the white region for CVE1-SL in Fig. 14. In this region, at high product pressure, the reaction may

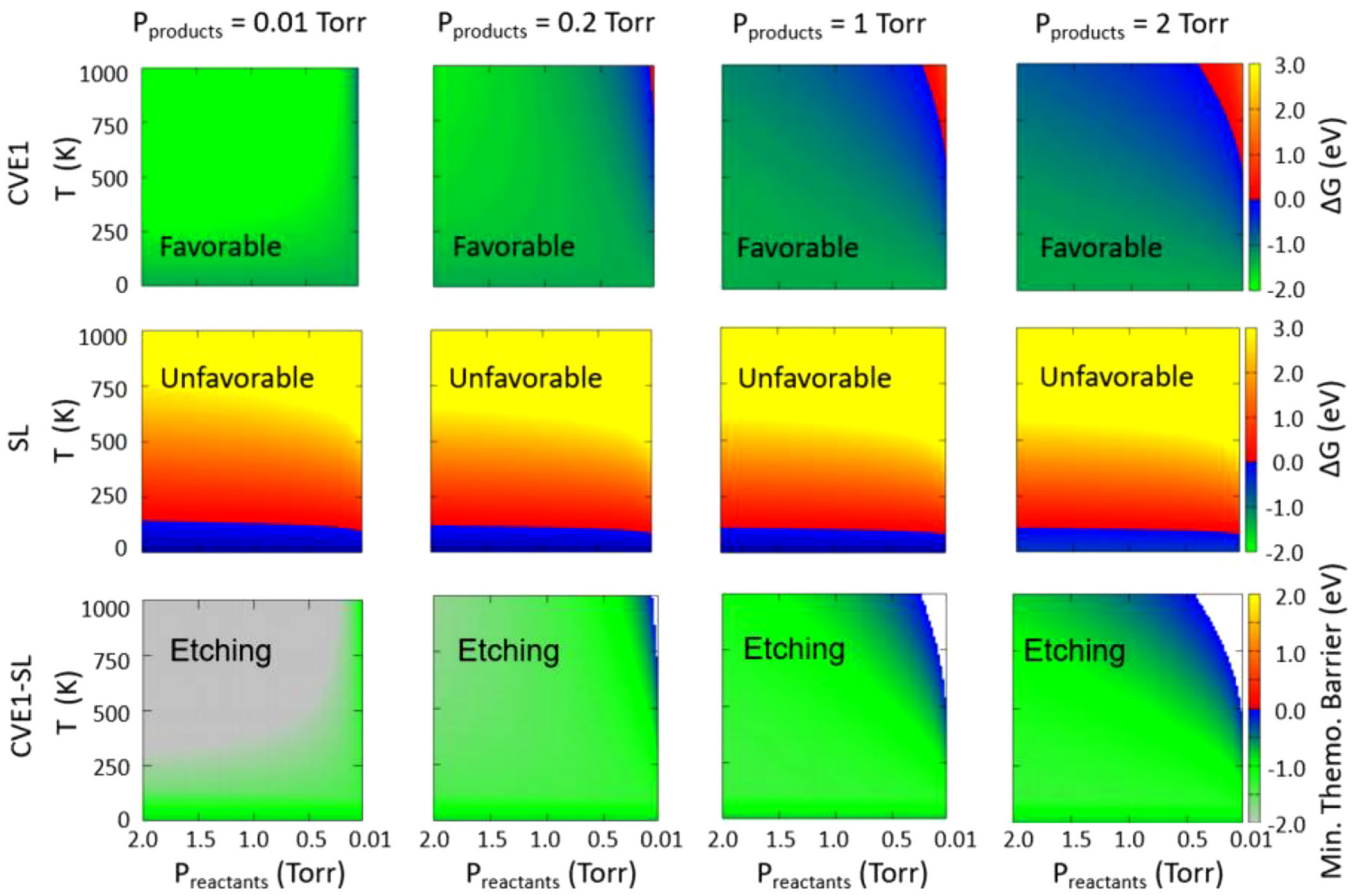

FIG. 14. 2D heat maps of ΔG free energies of CVE1 and SL reactions and corresponding "minimum thermodynamic barrier" to etch given by CVE1-SL with respect to change in HF pressure from 0.01 to 2.0 Torr for product pressures of 0.01, 0.2, 1, and 2 Torr. Plots in each row share the same color bar and *y* axis.

reverse and lead to B_2O_3 deposition by $2BF_3 + 3H_2O \rightarrow B_2O_3 + 6HF$. However, high product pressures may not stop the etching reaction if the reactant pressure is also maintained at a high value.

IV. CONCLUSIONS

The reaction of HF on B_2O_3 was investigated using FTIR to demonstrate the spontaneous etching and understand the surface chemistry, QMS to identify the etch products, and DFT to predict and understand the CVE reaction. Using B_2O_3 films grown using B_2O_3 ALD, FTIR spectroscopy observed the CVE of B_2O_3 by HF at 150 °C. B_2O_3 etching was monitored by the loss of absorbance for the B–O stretching vibration in B_2O_3 at 1200–1600 cm^{-1}. FTIR spectroscopy studies also observed B–F stretching vibrations from BF_x species on the B_2O_3 surface at 1440 cm^{-1} after HF exposures.

The volatile etch products during the spontaneous etching of B_2O_3 by HF at 150 °C were identified by QMS studies. The main etch products were BF_3, $B(OH)F_2$, and H_2O. During the initial HF exposures on B_2O_3 powders that had been exposed to air, boroxine ring etch products were also detected including $B_3O_3F_3$, $B_3O_3F_2(OH)$, and $B_3O_3F(OH)_2$. After etching through the initial hydrated B_2O_3 powder, the later HF exposures produced mostly BF_3 and H_2O and fewer $B(OH)F_2$ and boroxine ring products.

DFT studies investigated the energetics of the CVE reactions and SL reactions. The spontaneous etching of B_2O_3 was predicted at temperatures above −163 °C for an HF reactant pressure of 0.2 Torr and BF_3 and H_2O combined product pressure of 0.01 Torr. DFT calculations confirmed that BF_3 is the preferred etch product. In addition, the energetics of the reaction was affected slightly by the pressure of the reactant and products.

ACKNOWLEDGMENTS

The FTIR studies were funded by Intel through a member specific research grant through the Semiconductor Research Corporation (SRC). Support for the new QMS reactor and the QMS investigations was provided by Lam Research. S.K.N. and S.D.E. acknowledge the Irish Centre for High-End Computing (Project Code No. tiche077c) and the Science Foundation Ireland funded computing cluster at Tyndall for computer time.

DATA AVAILABILITY

The data that support the findings of this study are available within the article.

REFERENCES

[1]K. J. Kanarik, S. Tan, and R. A. Gottscho, J. Phys. Chem. Lett. **9**, 4814 (2018).
[2]H. Abe, M. Yoneda, and N. Fujiwara, Jpn. J. Appl. Phys. **47**, 1435 (2008).
[3]V. M. Donnelly and A. Kornblit, J. Vac. Sci. Technol. A **31**, 050825 (2013).
[4]D. E. Ibbotson, J. A. Mucha, D. L. Flamm, and J. M. Cook, J. Appl. Phys. **56**, 2939 (1984).
[5]H. F. Winters and J. W. Coburn, Appl. Phys. Lett. **34**, 70 (1979).
[6]G. T. A. Kovacs, N. I. Maluf, and K. E. Petersen, Proc. IEEE **86**, 1536 (1998).
[7]K. R. Williams, K. Gupta, and M. Wasilik, J. Microelectromech. Syst. **12**, 761 (2003).
[8]K. R. Williams and R. S. Muller, J. Microelectromech. Syst. **5**, 256 (1996).
[9]L. R. Arana, N. d. Mas, R. Schmidt, A. J. Franz, M. A. Schmidt, and K. F. Jensen, J. Micromech. Microeng. **17**, 384 (2007).
[10]H. F. Winters, J. Vac. Sci. Technol. A **3**, 700 (1985).
[11]H. F. Winters, J. Vac. Sci. Technol. B **3**, 9 (1985).
[12]H. F. Winters, J. Vac. Sci. Technol. A **3**, 786 (1985).
[13]J. K. C. Chen, N. D. Altieri, T. Kim, E. Chen, T. Lill, M. H. Shen, and J. P. Chang, J. Vac. Sci. Technol. A **35**, 05C305 (2017).
[14]M. A. George, D. W. Hess, S. E. Beck, J. C. Ivankovits, D. A. Bohling, and A. P. Lane, J. Electrochem. Soc. **142**, 961 (1995).
[15]M. A. George, D. W. Hess, S. E. Beck, K. Young, D. A. Bohling, G. Voloshin, and A. P. Lane, J. Electrochem. Soc. **143**, 3257 (1996).
[16]C. R. Helms and B. E. Deal, J. Vac. Sci. Technol. A **10**, 806 (1992).
[17]P. C. Lemaire and G. N. Parsons, Chem. Mater. **29**, 6653 (2017).
[18]A. Fischer, A. Routzahn, Y. Lee, T. Lill, and S. M. George, J. Vac. Sci. Technol. A **38**, 022603 (2020).
[19]S. M. George, Acc. Chem. Res. **53**, 1151 (2020).
[20]Y. Lee, J. W. DuMont, and S. M. George, Chem. Mater. **28**, 2994 (2016).
[21]Y. Lee, J. W. DuMont, A. S. Cavanagh, and S. M. George, J. Phys. Chem. C **119**, 14185 (2015).
[22]A. Lii-Rosales, A. S. Cavanagh, A. Fischer, T. Lill, and S. M. George, Chem. Mater. **33**, 7719 (2021).
[23]A. Fischer, A. Routzahn, S. M. George, and T. Lill, J. Vac. Sci. Technol. A **39**, 030801 (2021).
[24]S. M. George and Y. Lee, ACS Nano **10**, 4889 (2016).
[25]J. W. DuMont, A. E. Marquardt, A. M. Cano, and S. M. George, ACS Appl. Mater. Interfaces **9**, 10296 (2017).
[26]N. R. Johnson and S. M. George, ACS Appl. Mater. Interfaces **9**, 34435 (2017).
[27]Y. Lee and S. M. George, Chem. Mater. **29**, 8202 (2017).
[28]R. Mullins, S. Kondati Natarajan, S. D. Elliott, and M. Nolan, Chem. Mater. **32**, 3414 (2020).
[29]S. Kondati Natarajan and S. D. Elliott, Chem. Mater. **30**, 5912 (2018).
[30]J. W. DuMont and S. M. George, J. Phys. Chem. C **119**, 14603 (2015).
[31]J. D. Ferguson, A. W. Weimer, and S. M. George, Thin Solid Films **371**, 95 (2000).
[32]Y. Lee, J. W. DuMont, and S. M. George, ECS J. Solid State Sci. Technol. **4**, N5013 (2015).
[33]J. W. Clancey, A. S. Cavanagh, J. E. T. Smith, S. Sharma, and S. M. George, J. Phys. Chem. C **124**, 287 (2020).
[34]J. P. Perdew, K. Burke, and M. Ernzerhof, Phys. Rev. Lett. **77**, 3865 (1996).
[35]G. Kresse and J. Furthmuller, Phys. Rev. B **54**, 11169 (1996).
[36]G. Kresse and D. Joubert, Phys. Rev. B **59**, 1758 (1999).
[37]P. E. Blöchl, Phys. Rev. B **50**, 17953 (1994).
[38]A. Togo and I. Tanaka, Scr. Mater. **108**, 1 (2015).
[39]TURBOMOLE V6.2 2010, a development of University of Karlsruhe and Forschungszentrum Karlsruhe GmbH, 1989–2007, TURBOMOLE GmbH, since 2007, see http://www.turbomole.com.
[40]K. Persson, Materials Data on B_2O_3 (SG:152), 2014: Materials Project.
[41]M. Putkonen and L. Niinistö, Thin Solid Films **514**, 145 (2006).
[42]J. S. Ogden and N. A. Young, J. Chem. Soc. Dalton Trans. **6**, 1645 (1988).
[43]J. L. Parsons, J. Chem. Phys. **33**, 1860 (1960).
[44]K. T. Queeney, M. K. Weldon, J. P. Chang, Y. J. Chabal, A. B. Gurevich, J. Sapjeta, and R. L. Opila, J. Appl. Phys. **87**, 1322 (2000).
[45]A. S. Tenney and J. Wong, J. Chem. Phys. **56**, 5516 (1972).
[46]G. L. Vick and K. M. Whittle, J. Electrochem. Soc. **116**, 1142 (1969).
[47]D. Peak, G. W. Luther, and D. L. Sparks, Geochim. Cosmochim. Acta **67**, 2551 (2003).
[48]R. E. Scruby, J. R. Lacher, and J. D. Park, J. Chem. Phys. **19**, 386 (1951).
[49]Y. Gong and M. F. Zhou, J. Phys. Chem. A **112**, 5670 (2008).
[50]P. Ayotte, M. Hebert, and P. Marchand, J. Chem. Phys. **123**, 184501 (2005).
[51]J. W. DuMont and S. M. George, J. Chem. Phys. **146**, 052819 (2017).
[52]D. A. Dows, J. Chem. Phys. **31**, 1637 (1959).
[53]L. M. Nxumalo and T. A. Ford, Vib. Spectrosc. **6**, 333 (1994).
[54]P. Saenz, R. E. Cachau, G. Seoane, M. Kieninger, and O. N. Ventura, J. Phys. Chem. A **110**, 11734 (2006).
[55]C. J. Ultee, J. Chem. Phys. **40**, 3746 (1964).
[56]R. F. Porter, D. R. Bidinosti, and K. F. Watterson, J. Chem. Phys. **36**, 2104 (1962).
[57]D. R. Bidinosti and L. L. Coatsworth, Can. J. Chem. **48**, 2484 (1970).